Acta Acustica united with Acustica
Vol. 93 (2007) 944 – 958

Estimates of the relevant turbulent scales for acoustic propagation in an upward refracting atmosphere

Benjamin Cotté, Philippe Blanc-Benon
Laboratoire de Mécanique des Fluides et d'Acoustique, UMR CNRS 5509, École Centrale de Lyon, 69134 Ecully Cedex, France, benjamin.cotte@ec-lyon.fr

Summary
Turbulent fluctuations of temperature and velocity in the atmospheric boundary layer play a significant role on acoustic propagation, especially when an acoustic shadow zone is present. Spatial scales of turbulence span many orders of magnitude, and it has been recognized that some of them scatter acoustic energy more effectively. This selection of relevant turbulent scales depends on propagation geometry and acoustic frequency. The goal of this paper is to estimate the extent of the turbulence spectrum that contributes to acoustic scattering into a refractive shadow zone. The study is based on elements of wave propagation in random media theory on the one hand, and parabolic equation (PE) simulations on the other hand. To be representative of transportation and industrial noise conditions, PE simulations are performed in third octave bands between 50 Hz and 1600 Hz; the maximum propagation distance is 1 km. The turbulent fields are generated using a random Fourier modes technique. Theoretical tools are used to analyze the numerical results. Concerning small structures, an expression for the maximum cut-off turbulent wave number is obtained from the characteristics of the scattering cross-section. Concerning large structures, an estimate of the minimum cut-off turbulent wave number involving the Fresnel radius is found; it is based on the form of the variance of log-amplitude fluctuations in the Rytov approximation. This estimate is valid when the scattering is unsaturated, i.e. when the propagation distance and acoustic frequency are relatively small. The relations presented here may be used for modelling purposes and for experimental data analysis to know if the measured turbulent spectra cover a wide enough range of spatial scales in a given configuration.

PACS no. 43.28.Fp, 43.20.Fn

1. Introduction

It is well-known that turbulent fluctuations of temperature and velocity in the atmosphere have a strong influence on acoustic propagation when an acoustic shadow zone is present. This situation is not uncommon; it happens in the presence of a negative temperature gradient (thermal lapse conditions), typical of a sunny day, in the case of upwind propagation, or when the receiver is behind a hill or a noise barrier. The situation studied in this paper corresponds to a refractive shadow zone (flat ground), and is sketched in Figure 1. In the context of transportation and industrial noise predictions, source and receivers are relatively close to the ground, and the propagation distance is usually less than 1 km.

In the atmospheric boundary layer, spatial scales span many orders of magnitude, from millimeters to kilometers, and some of them scatter acoustic energy more effectively. An example is given by Stinson *et al.* [1], who performed parabolic equation simulations in an upward refracting atmosphere at an acoustic frequency of 500 Hz, and showed that turbulent length scales between 2 and 5 m are most effective for scattering. Also, some scattering properties are described by the theory of wave propagation in random media [2, 3, 4, 5], which shows that there is a coupling between turbulent scales, geometry and acoustic frequency. This theory has been used extensively for remote sensing of the atmosphere [6, 7, 8]. For example, Stinson *et al.* explained their numerical results thanks to simple Bragg's scattering considerations. Gilbert *et al.* [9] used a distorted-wave Born approximation analysis and formulated the scattering problem in terms of a "sampling function" that filters the turbulence spectrum. Wilson *et al.* [10] also noticed that "the propagation geometry and acoustic frequency combine to create a filter that selects a specific part of the turbulence spectrum participating in the scattering". That is how they explained that different authors could have obtained acoustic predictions in reasonable agreement with measurements using different spectral models (Gaussian, Kolmogorov, von Kármán, etc.).

Nevertheless, little is known on the actual extent of the turbulence spectrum that is "acoustically filtered". This pa-

Received 20 March 2007, revised 15 June 2007, accepted 18 June 2007.

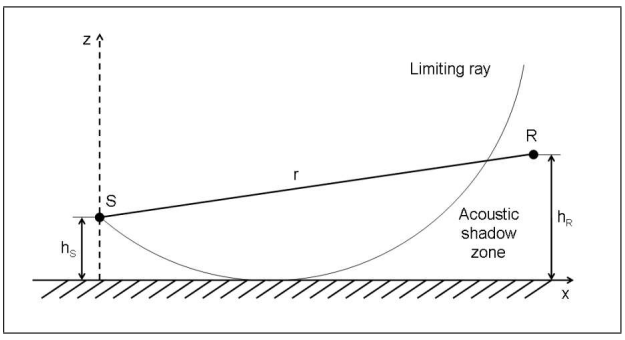

Figure 1. Geometry of the problem. The limiting ray is the ray that grazes the ground in the geometric approximation.

per is aimed at giving estimates of the turbulent scales involved in the scattering of sound. This is done in the context of traffic and industrial noise propagation, thus the emphasis is on sound pressure level (or amplitude) fluctuations rather than phase fluctuations. Note that these estimates are useful in numerical simulations, to take into account the relevant turbulent scales without modelling the entire turbulence spectrum. They can also be useful in experiments to know whether the sensors resolution and averaging periods chosen to measure wind speed and temperature fluctuations enable to cover a wide enough range of turbulent scales (see for instance [11] on the influence of sensors resolution, and [10, 12] on the influence of averaging periods).

The coupling between turbulence scales, geometry and acoustic frequency is first studied in section 2 using theoretical tools from the wave propagation in random media literature. It will be seen that temperature and velocity fluctuations do not have the same scattering properties [13, 14]. It will also be shown that the scattering regimes can be different depending on the propagation distance and acoustic frequency considered. Then the role of small and large-scale turbulent fluctuations are studied using parabolic equation (PE) simulations in section 3. PE simulations are performed in third octave bands between 50 Hz and 1600 Hz. This is a major difference with previous studies where pure tones were usually considered. Finally, estimates of the smallest and largest turbulent scales involved in acoustic scattering are derived based on the theoretical and numerical results.

2. Theoretical background

The basic assumptions and turbulence models used in this paper are first presented in section 2.1. Then classical results from wave propagation in random media are presented, namely the scattering cross-section for single scattering in section 2.2, and the variances of log-amplitude and phase fluctuations in the Rytov approximation in section 2.4. These expressions relate turbulent scales to acoustic frequency and geometry, and will be used in section 3 to estimate the smallest and largest turbulent structures involved in acoustic scattering. The simulations performed in section 3 are also placed in Flatté's $\Lambda - \Phi$ diagram [15] in section 2.3 to determine which scattering regimes they correspond to and whether the Rytov approximation is valid or not. All the expressions are written in a three-dimensional domain.

2.1. Turbulence modelling

In this paper, scattering by temperature and velocity fluctuations are studied. The Markov approximation is supposed to be valid, which means that the longitudinal correlation length of the sound field is large with respect to the size of the inhomogeneities in the medium. This implies that there is a main direction of propagation, say x, where $\mathbf{r} = (x, y, z)$ (see [4, 5] for more details on the Markov approximation). Temperature and velocity fluctuations can be written in terms of index of refraction fluctuations μ, where $n = c_0/c = \overline{n} + \mu$ is the index of refraction, c the sound speed and c_0 a reference sound speed ($\mu \ll 1$). The variance of the index of refraction fluctuations $\overline{\mu^2}$ is related to the variance of temperature fluctuations $\overline{T'^2}$ and velocity fluctuations $\overline{V_x'^2}$ by

$$\overline{\mu^2} \approx \frac{\overline{T'^2}}{4T_0^2} + \frac{\overline{V_x'^2}}{c_0^2}, \tag{1}$$

with T_0 the reference temperature related to c_0. Let $\mathbf{K} = (K_x, \mathbf{K}_\perp)$ be the turbulent wave number, with $\mathbf{K}_\perp = (K_y, K_z)$ its component in the plane perpendicular to x. The spectral density of index of refraction fluctuations $\Phi_n(K_x, \mathbf{K}_\perp)$ is related to the spectral densities of temperature fluctuations $\Phi_T(K_x, \mathbf{K}_\perp)$ and velocity fluctuations $\Phi_{xx}(K_x, \mathbf{K}_\perp)$ by

$$\Phi_n(K_x, \mathbf{K}_\perp) = \frac{\Phi_T(K_x, \mathbf{K}_\perp)}{4T_0^2} + \frac{\Phi_{xx}(K_x, \mathbf{K}_\perp)}{c_0^2}. \tag{2}$$

In the Markov approximation: $\Phi_n(K_x, \mathbf{K}_\perp) = \Phi_n(0, \mathbf{K}_\perp)$. Furthermore, the turbulence is supposed to be homogeneous and isotropic in the following, thus the spectral densities only depend on $K = |\mathbf{K}_\perp|$, and

$$\Phi_n(K) = \frac{1}{4T_0^2}\frac{G(K)}{4\pi K^2} + \frac{1}{c_0^2}\frac{E(K)}{4\pi K^2}, \tag{3}$$

where $G(K)$ and $E(K)$ are the three-dimensional spectra of thermal turbulent energy and kinetic turbulent energy, respectively.

These spectra can be modelled by a modified von Kármán spectrum [3, 5]:

$$G(K) = A\frac{\overline{T'^2}}{L_0^{2/3}} K^2 \left(K^2 + \frac{1}{L_0^2}\right)^{-11/6} \mathrm{e}^{-K^2/K_m^2}, \tag{4}$$

$$E(K) = \frac{11}{6} A\frac{\overline{V_x'^2}}{L_0^{2/3}} K^4 \left(K^2 + \frac{1}{L_0^2}\right)^{-17/6} \mathrm{e}^{-K^2/K_m^2}, \tag{5}$$

with $A = 0.792$, $K_m = 5.92/l_0$, and with L_0 and l_0 the outer and inner scales of turbulence, respectively. These

spectra can also be written in terms of the structure parameters C_T^2 and C_v^2 for temperature and velocity fluctuations, respectively [3, 5]: $C_T^2 = B\overline{T'^2}L_0^{-2/3}$ and $C_v^2 = B\overline{V_x'^2}L_0^{-2/3}$ with $B = 1.91$. In this study, the parameters of the turbulence spectra are $L_0 = 5\,m$, $l_0 = 0.05\,m$, and $\overline{\mu^2} = 10^{-5}$. This value of $\overline{\mu^2}$ corresponds to a temperature standard deviation of 1.8 K and a velocity standard deviation of 1.1 m/s. The three-dimensional spectra of turbulent energy written in terms of index of refraction fluctuations are plotted in Figure 2. One can notice that temperature fluctuations are stronger than velocity fluctuations in the energy subrange ($K < 0.2\,\mathrm{m}^{-1}$ with the parameters chosen), while velocity fluctuations are stronger in the inertial and dissipation subranges ($K > 0.2\,\mathrm{m}^{-1}$).

2.2. Scattering cross-section

The scattering cross-section characterizes the amount of acoustic power scattered by a volume of inhomogeneities (or scattering volume) per unit incident acoustic intensity and per unit volume [5, 16]:

$$\sigma = \frac{r^2 \bar{I}_s}{I_0 V}. \tag{6}$$

$\bar{I}_s$ is the mean scattered acoustic intensity, I_0 is the incident acoustic intensity, and the notations of Figure 3 are used. For homogeneous and isotropic turbulence, the general form of the scattering cross-section is [5, 16]:

$$\sigma(\theta) = \frac{k^2}{8}\frac{\cos^2\theta}{\sin^2\theta/2}\left[\frac{1}{4T_0^2}G(2k\sin\theta/2) + \frac{\cos^2\theta/2}{c_0^2}E(2k\sin\theta/2)\right], \tag{7}$$

where $k = 2\pi/\lambda$ is the acoustic wave number, and λ is the acoustic wavelength. The derivation of equation (7) is given in the Appendix. Bragg's scattering is assumed, which means that the acoustic wave is single scattered by the volume of inhomogeneities, and the distances r_0 and r are supposed to be large with respect to the linear size L of the scattering volume V. Thus equation (7) holds for $r_0, r \gg L \gg \lambda$; it does not depend on the waveform. Equation (7) shows that scattering at the angle θ depends mainly on turbulent structures with associated wave numbers $K = 2k\sin\theta/2$, which is known as Bragg's relation. This is an important result that can be used to relate turbulent scales to acoustic frequencies, as will be done in section 3.

Combining equations (4), (5) and (7), an analytical expression can be given for the scattering cross-section associated with a modified von Kármán spectrum:

$$\sigma(\theta) = \frac{2^{-20/3}AL_0^{-2/3}k^{1/3}\cos^2\theta}{\left(\sin^2\theta/2 + (2kL_0)^{-2}\right)^{11/6}}D(k,\theta) \cdot \left[\frac{\overline{T'^2}}{T_0^2} + \frac{11}{6}\frac{\overline{V_x'^2}}{c_0^2}\frac{\sin^2\theta}{\sin^2\theta/2 + (2kL_0)^{-2}}\right], \tag{8}$$

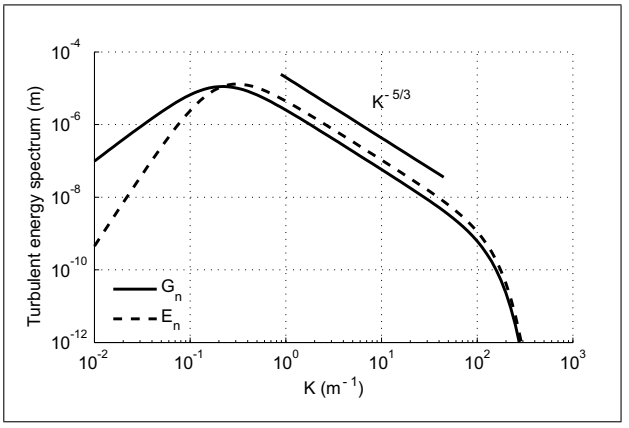

Figure 2. Three-dimensional spectra of thermal turbulent energy $G_n = G/(4T_0^2)$ and kinetic turbulent energy $E_n = E/c_0^2$ written in terms of index of refraction fluctuations.

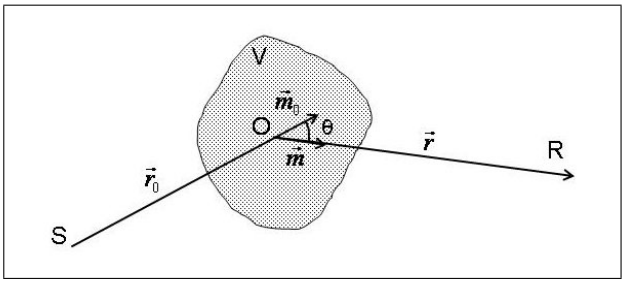

Figure 3. Geometry for Bragg's scattering. V is the scattering volume and θ is the scattering angle.

with $D(k,\theta) = \exp(-4k^2\sin^2(\theta/2)/K_m^2)$. Equation (8) is equation (21) of [17], where K_m is assumed to be large so that $D(k,\theta) \approx 1$. $D(k,\theta)$ is related to the dissipation scales of turbulence, and can be approximately set to 1 when $\lambda/(2\sin\theta/2) \gg l_0$. This inequality is generally valid in atmospheric acoustics. To normalize the scattering cross-section, let's introduce the total scattering cross-section σ_0, defined as [5, 16]:

$$\sigma_0 = \oint \sigma(\mathbf{n})\,\mathrm{d}\Omega(\mathbf{n}) = \int_0^{2\pi}\mathrm{d}\phi\int_0^{\pi}\sigma(\theta)\sin\theta\,\mathrm{d}\theta, \tag{9}$$

with $d\Omega(\mathbf{n})$ the solid angle in the direction of the unit vector $\mathbf{n}$. σ_0 is the total scattering power removed from the incident wave per unit distance. It is also related to the extinction coefficient γ, defined as $\overline{p} = \exp(-\gamma x)p_0$, where $\overline{p}$ is the mean field and p_0 the incident field [4, 5]:

$$\sigma_0 = 2\gamma = 4\pi^2k^2\int_0^{\infty}K\Phi_n(K)\,\mathrm{d}K. \tag{10}$$

Ostashev [5] shows that equation (10) is valid for motionless and moving random media. For a modified von Kármán spectrum, the total scattering cross-section is:

$$\sigma_0 = \frac{3}{5}\pi Ak^2L_0\left(\frac{\overline{T'^2}}{4T_0^2} + \frac{\overline{V_x'^2}}{c_0^2}\right). \tag{11}$$

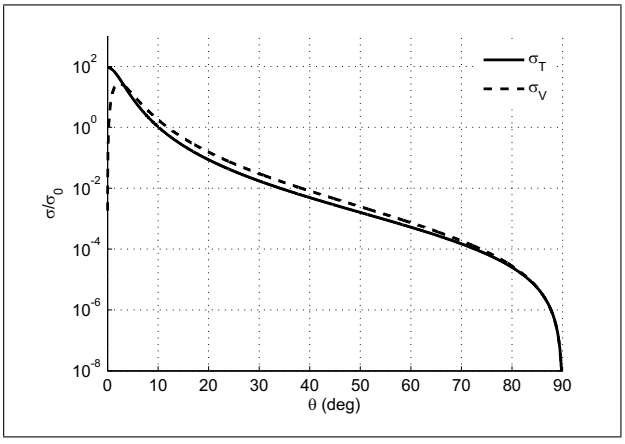

Figure 4. Normalized cross-section σ/σ_0 at 200 Hz for temperature (solid line) and velocity (dashed line) fluctuations.

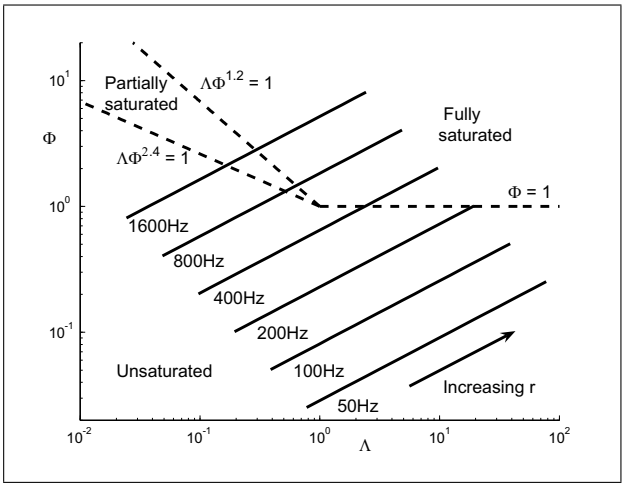

Figure 5. $\Lambda - \Phi$ diagram. The scattering regions are separated by dashed lines. The solid lines correspond to acoustic frequencies between 50 and 1600 Hz (as labelled), with ranges r between 10 and 1000 m.

To obtain this result, the integration in equation (10) is calculated using confluent hypergeometric functions (see for instance Appendix D of [3]).

The scattering cross-section can be split into two contributions: $\sigma = \sigma_T + \sigma_V$, where σ_T is due to temperature fluctuations and σ_V is due to velocity fluctuations. The normalized scattering cross-section σ/σ_0 for these two contributions is plotted in Figure 4 at 200 Hz. It appears that the behaviors of σ_V and σ_T differ mostly at small scattering angles. For forward scattering ($\theta = 0$), σ_V is zero while σ_T reaches a maximum. At higher scattering angles, the normalized scattering cross-section is higher for velocity fluctuations than for temperature fluctuations. Expressions for the scattering cross-section in a two-dimensional domain are derived in the Appendix. Using a modified von Kármán spectrum to model turbulent fluctuations, an expression similar to equation (8) is obtained. It appears that the dependence of the scattering cross-section on scattering angle is the same in two and three dimensions. This is an important result since PE simulations used in section 3 are performed in a two-dimensional domain.

2.3. Scattering regimes in the $\Lambda - \Phi$ diagram

Scattering by atmospheric turbulence can follow different characteristics, or regimes, depending on the geometry and acoustic frequency considered. These scattering regimes can be looked at in the $\Lambda - \Phi$ diagram, as introduced by Flatté *et al.* [15, Chap. 6]. The $\Lambda - \Phi$ diagram can also be used to assess the validity of the Rytov approximation used in section 2.4. The strength parameter Φ and the diffraction parameter Λ are defined as [15, 18]:

$$\Phi^2 = 2L_T k^2 r\overline{\mu^2}, \tag{12}$$

$$\Lambda = r/(kL_T^2), \tag{13}$$

where $L_T = L_0/1.339$ is the integral scale. Depending on the value of these parameters, the scattering is referred to as "unsaturated", "saturated", or "partially saturated" (see Figure 5). The limits between the three scattering regions are determined using an energy spectrum with a power law $K^{-5/3}$ [15, 18] (Kolmogorov spectrum or, equivalently, von Kármán spectrum in the inertial range). In the unsaturated region (small Φ), one micropath reaches the receiver (single scattering) and the Rytov approximation of smooth perturbations is valid. In the saturated and partially saturated region (large Φ), multipath propagation occurs, and the Rytov approximation breaks down. In the partially saturated region, Λ is small and the micropaths are correlated, while in the fully saturated region, Λ is large and the micropaths are uncorrelated.

The PE simulations studied in section 3 are performed for frequencies between 50 Hz and 1600 Hz and a maximum range of 1000 m. The associated $\Lambda - \Phi$ pairs are plotted in Figure 5. It appears that for large ranges and high frequencies, the simulations correspond to saturated scattering conditions, which means that the Rytov approximation is not valid anymore. Let $r_{sat}(f)$ be the limiting range between the unsaturated region and one of the saturated regions, and f_{lim} the acoustic frequency for which $\Lambda = \Phi = 1$ (intersection between the three scattering zones):

$$f_{lim} = c_0 / \left[2\pi L_T \left(2\overline{\mu^2} \right)^{1/3} \right], \tag{14}$$

$$r_{sat}(f_{lim}) = L_T / \left(2\overline{\mu^2} \right)^{1/3}. \tag{15}$$

With the turbulence spectrum defined in section 2.1, $f_{lim} = 534\,Hz$ and $r_{sat}(f_{lim}) = 138\,m$. When $f \leq f_{lim}$, the scattering goes directly from no saturation to full saturation as the range increases (see Figure 5), and the limiting range is found solving $\Phi = 1$. When $f \geq f_{lim}$, the scattering passes through the partially saturated region as the range increases and the limiting range is found solving $\Lambda\Phi^{2.4} = 1$. Thus:

$$r_{sat} = \begin{cases} 1/\left(2L_T k^2 \overline{\mu^2} \right) & \text{if } f \leq f_{lim}, \\ \left[{L_T}^{0.8} / \left(2^{1.2} k^{1.4} \overline{\mu^2}^{1.2} \right) \right]^{1/2.2} & \text{if } f \geq f_{lim}, \end{cases} \tag{16}$$

The third octave band spectrum of r_{sat} is plotted in Figure 6. r_{sat} decreases rapidly with acoustic frequency, becoming less than 1000 m above 200 Hz and less than 200 m above 500 Hz. Since the Rytov approximation is valid for $r < r_{sat}$, this strongly limits the use of the Rytov approximation at the highest frequencies considered in this paper.

2.4. Variance of log-amplitude and phase fluctuations in the Rytov approximation

In this section, the variances of log-amplitude and phase fluctuations in the Rytov approximation of smooth perturbations are presented. Let $\psi(\mathbf{r})$ be the eikonal of the scattered pressure $p(\mathbf{r}) = A(\mathbf{r})\exp(S(\mathrm{i}\mathbf{r}))$:

$$\begin{aligned}\psi(\mathbf{r}) &= \chi(\mathbf{r}) + \mathrm{i}\phi(\mathbf{r}) \\ &= \ln\left(\frac{A(\mathbf{r})}{A_0(\mathbf{r})}\right) + \mathrm{i}\big(S(\mathbf{r}) - S_0(\mathbf{r})\big),\end{aligned} \tag{17}$$

where $\chi(\mathbf{r})$ and $\phi(\mathbf{r})$ are respectively the fluctuations of the log-amplitude and the phase with respect to the incident wave (with the subscript zero). The variances of log-amplitude and phase fluctuations can be deduced from the correlation functions $B_\chi(r, \rho)$ for the log-amplitude and $B_\phi(r, \rho)$ for the phase at lag $\rho = 0$. They have the general form [2, 4, 5]:

$$\overline{\chi^2}, \overline{\phi^2} = 2\pi^2 k^2 r \int_0^\infty f_{\chi,\phi}(K^2/K_F^2)\, K\, \Phi_n(K)\, \mathrm{d}K, \tag{18}$$

with $K_F^2 = k/r$ (K_F is inversely proportional to the radius of the first Fresnel zone), and Φ_n as given in equation (3). Equation (18) shows the existence of a function $f_{\chi,\phi}$ of K^2/K_F^2 that filters the turbulence spectrum. This filtering function depends on the waveform. For spherical wave propagation:

$$f_{\chi,\phi}(K^2/K_F^2) = \int_0^1 \left[1 \mp \cos\left(\eta(1-\eta)K^2/K_F^2\right)\right] \mathrm{d}\eta. \tag{19}$$

The filtering functions f_χ and f_ϕ are evaluated numerically and plotted in Figure7. When K^2/K_F^2 approaches zero, f_χ approaches zero while f_ϕ approaches its maximum value of 2. This means that part of the large turbulent structures will not contribute to the variance of log-amplitude fluctuations $\overline{\chi^2}$.

To characterize the dependence of this large structures filtering on acoustic frequency and geometry, an approximate analytical expression for $f_{\chi,\phi}$ is derived. Introducing the approximation

$$\eta(1-\eta) \approx \begin{cases} \eta/2 & \text{if } 0 \le \eta \le 1/2, \\ (1-\eta)/2 & \text{if } 1/2 \le \eta \le 1, \end{cases} \tag{20}$$

in equation (19), the filtering function becomes:

$$f_{\chi,\phi}(K^2/K_F^2) \approx 1 \mp \frac{\sin(K^2/4K_F^2)}{K^2/4K_F^2}. \tag{21}$$

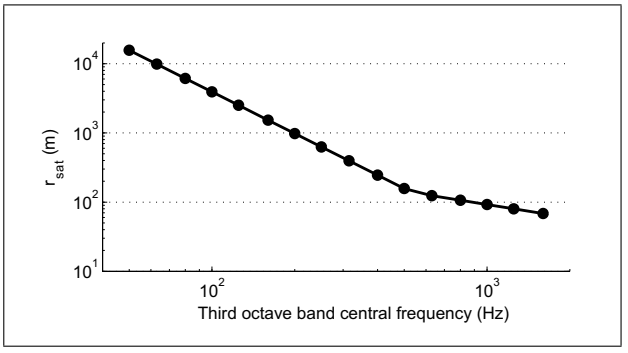

Figure 6. Third octave band spectrum of the limiting range r_{sat} between the unsaturated region and one of the saturated regions (see Figure 5).

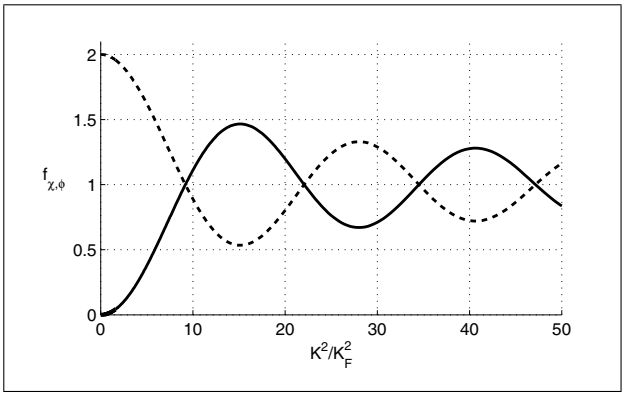

Figure 7. Filtering functions f_χ (solid lines) and f_ϕ (dashed lines) with respect to K^2/K_F^2.

Table I. Values of K_1, the first zero of $f_{\chi,\phi} - 1$. The exact solution is estimated numerically from equation (19), and the approximate solution is calculated with equation (22).

Acoustic frequency (Hz)		100	200	400
K_1 (m^{-1}) at $r = 250\,m$	exact	0.26	0.37	0.52
	approximate	0.30	0.43	0.61
K_1 (m^{-1}) at $r = 500\,m$	exact	0.18	0.26	-
	approximate	0.22	0.30	-

Let K_1 be the first zero of $f_{\chi,\phi} - 1$. From equation (21):

$$K_1 \approx 2\sqrt{\pi}K_F = 2\sqrt{2}\pi/\sqrt{\lambda r}. \tag{22}$$

Values of K_1 estimated numerically and calculated with equation (22) are compared in Table I for different ranges and acoustic frequencies. For a range of 500 m and a frequency of 400 Hz, no estimates are given since the Rytov approximation beaks down (see section 2.3). Table I shows that equation (22) overestimates K_1 by 17% for the ranges and acoustic frequencies considered. As a result, as given in equation (22), K_1 is proportional to K_F or inversely proportional to $\sqrt{\lambda r}$. This property will be used in section 3.3 to estimate the minimum cut-off turbulent wave number.

The variances of log-amplitude and phase fluctuations are evaluated numerically and plotted in Figure 8 at the

acoustic frequencies of 100 Hz, 200 Hz and 400 Hz. The calculations are made only for the ranges $r \leq r_{sat}$, with r_{sat} given in equation (16). Figure 8 shows that phase fluctuations are approximately the same for both temperature and velocity fluctuations. On the other hand, log-amplitude fluctuations are greater for velocity fluctuations than for temperature fluctuations. The variances of log-amplitude and phase fluctuations in a two-dimensional domain are presented in the Appendix. The filtering functions that appear are the same as those given in equation (19), which shows that the influence of large-scale turbulent fluctuations is similar in two and three dimensions.

3. Estimates of relevant cut-off turbulent wave numbers

3.1. Parabolic Equation simulations

Acoustic propagation in a turbulent atmosphere can be modelled using parabolic equation methods. In the classical formulation, called Wide Angle Parabolic Equation (WAPE), the moving atmosphere is modelled by a hypothetical motionless medium with the effective sound speed $c_{eff} = c + V'_x$. More recently, other formulations have been proposed that maintain the vector properties of the velocity field [14, 19]. In this study, simulations are based on one of these formulations, the Mean Wind Wide Angle Parabolic Equation (MW-WAPE) [20]. They are performed in a two-dimensional domain. In the MW-WAPE formulation, the pressure field $p(\mathbf{r})$ is the solution of

$$\frac{\partial p}{\partial x} = \mathrm{i}k_0 \left(1 + \mathcal{F} + \mathcal{M}\frac{\partial}{\partial x}\right)^{1/2} p, \tag{23}$$

with $k_0 = 2\pi f/c_0$ and

$$\mathcal{F} = (n^2 - 1) + \frac{1}{k_0^2}\frac{\partial^2}{\partial z^2} + \frac{2in^2}{k_0}\frac{V'_z}{c_0}\frac{\partial}{\partial z} + \frac{V'^2_x}{c_0^2}\left(1 + \frac{1}{k_0^2}\frac{\partial^2}{\partial z^2}\right) - \frac{1}{k_0^2}\frac{V'^2_z}{c_0^2}\frac{\partial^2}{\partial z^2}, \tag{24}$$

$$\mathcal{M} = \frac{2in^2}{k_0}\frac{V'_x}{c_0} - \frac{2}{k_0^2}\frac{V'_x V'_z}{c_0^2}\frac{\partial}{\partial z}, \tag{25}$$

where $n = c_0/c = \bar{n} + \mu$ is the index of refraction. These equations are derived keeping terms of $\mathcal{O}(M^2)$, $\mathcal{O}(\mu M)$ and $\mathcal{O}(\mu^2)$, with μ the index of refraction fluctuation and $M = |\mathbf{V}'|/c_0$ the Mach number. Also, the acoustic wavelength λ is supposed to be small with respect to the characteristic scale of inhomogeneities in the medium L [5, 14, 19]. In the simulations presented hereafter, the condition $\lambda \ll L$ is not strictly met over the whole range of turbulent scales considered. However, Dallois and Blanc-Benon [21, 22] showed that this condition can be somewhat relaxed. They studied the scattering of acoustic waves by a vortex of characteristic size $L = \lambda/4$, and obtained very good agreement between the MW-WAPE solution and a direct numerical solution of the linearised Euler's equations. Therefore, it seems that a good accuracy can be achieved in the PE simulations even when the restriction $\lambda \ll L$ is not strictly met.

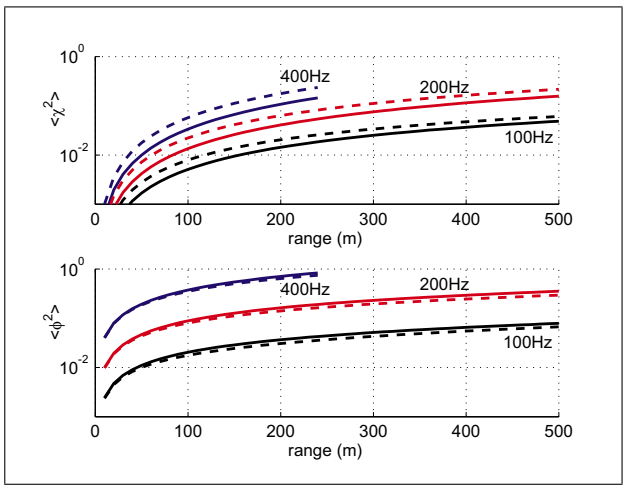

Figure 8. Variance of log-amplitude fluctuations $\overline{\chi^2}$ and phase fluctuations $\overline{\phi^2}$ in the Rytov approximation for temperature (solid lines) and velocity (dashed lines) fluctuations.

In order to obtain sound pressure level predictions in third octave bands between 50 Hz and 1600 Hz, several frequencies per band are calculated. As frequency increases, the width of the third octave band increases such that more frequencies need to be calculated within the band to keep a good accuracy; as a result 46 frequencies are calculated to obtain a complete third octave band spectrum. For all PE simulations presented in this paper, the source height is 2 m, and the ground impedance is calculated using the Delany and Bazley model [23] with an effective flow resitivity of 200 $kN\,sm^{-4}$, typical of grassland. Also, the sound speed profile is $c(z) = c_0 + a\ln(1 + z/z_0)$, with $c_0 = 340\,m/s$, $a = -2.1\,s^{-1}$ and $z_0 = 0.1\,m$. This sound speed profile is representative of a strong sound speed gradient. With this profile, the receiver is in the acoustic shadow zone in the first 500 m of propagation for third octave bands above 160 Hz. Thus, a range of 500 m is used in the simulations for these bands, while a range of 1 km is used for third octave bands below 125 Hz.

The turbulence fields are generated using a random Fourier modes technique assuming frozen turbulent fluctuations. This technique is described in [24] for temperature fluctuations and in [14, 19] for velocity fluctuations. The turbulent temperature field enters the PE through the index of refraction fluctuation $\mu = -T'/2T_0$. The turbulent velocity fields V'_x and V'_z are directly included in the PE, as seen in equations (24) and (25); it must be emphasized that the effective sound speed approximation is not used. The turbulent fluctuations are obtained by summation over the random Fourier modes, whose amplitude and phase are chosen to follow the spectral models presented in section 2.1. The Fourier modes are logarithmically distributed between a minimum turbulent wave number K_{min} and a maximum turbulent wave number K_{max}. The sound pressure is then calculated by averaging over

several realizations of the turbulence fields. In the following, most results are plotted in terms of relative sound pressure level, defined as $\Delta L = L_p - L_{p,free}$, where L_p is the calculated sound pressure level and $L_{p,free}$ is the sound pressure level in a homogeneous atmosphere in free field conditions. Varying K_{min} and K_{max} in the PE simulations, one can test the influence of different turbulent scales on acoustic scattering. Based on these numerical results and on theoretical results presented in section 2, cut-off turbulent wave numbers K_{Cmin} and K_{Cmax} can be estimated, corresponding respectively to the smallest and largest turbulent structures involved in acoustic scattering. Before estimating the maximum cut-off turbulent wave number in section 3.2 and the minimum cut-off turbulent wave number in section 3.3, we will briefly comment on the choice of the number of Fourier modes and the number of realizations in the simulations.

Since K_{min} and K_{max} can vary between simulations, it makes more sense to keep the density of modes (number of modes per decade of turbulent wave number) constant rather than the total number of modes. Simulations with 100 and 200 modes per decade of turbulent wave number are compared in Figure 9, where the relative sound pressure level is plotted with respect to height at a range of 300 m and on the 1000 Hz third octave band; 30 realizations of turbulence are used in these simulations. The solution in the absence of turbulence is also plotted for comparison. Close to the ground, the receiver is deep in the shadow zone, and the result is not very sensitive to the difference in mode density. However, for higher receivers located in the penumbra region, differences of 2 to 3 dB can occur. Similar results are obtained on other third octave bands, thus 100 modes per decade of turbulent wave number might not be enough to obtain reliable predictions for all receiver positions. In the following, 200 modes per decade of turbulent wave number will be used in the PE simulations.

When comparing PE simulations with different numbers of realizations of the turbulence fields, it appears that the largest differences occur at high frequency and relatively far from the ground. Thus, in Figure 10, the relative sound pressure level calculated with 25 and 30 realizations is plotted with respect to range at a height of 25 m and on the 1600 Hz third octave band. Levels are very close for temperature fluctuations, and there are differences of up to 2 dB for velocity fluctuations. As a result, 30 realizations of the turbulence fields seem enough to calculate the mean acoustic field.

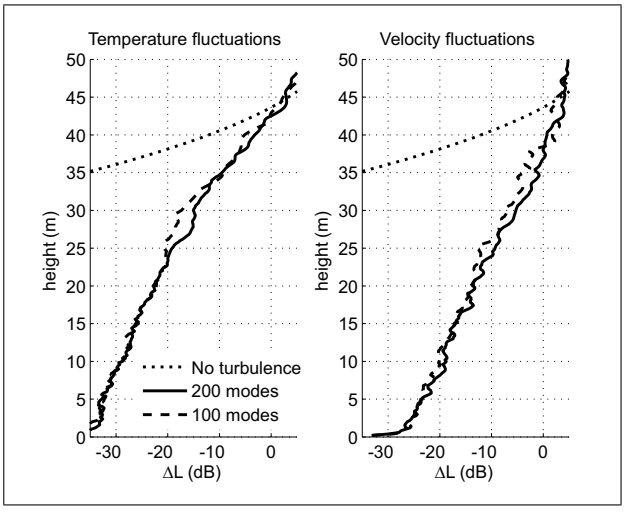

Figure 9. Relative sound pressure level ΔL at a range of 300 m and on the 1000 Hz third octave band for temperature (left) and velocity (right) fluctuations. ΔL is calculated using 100 or 200 modes per decade of turbulent wave number ($K_{min} = 0.15\,\mathrm{m}^{-1}$ and $K_{max} = 32\,\mathrm{m}^{-1}$).

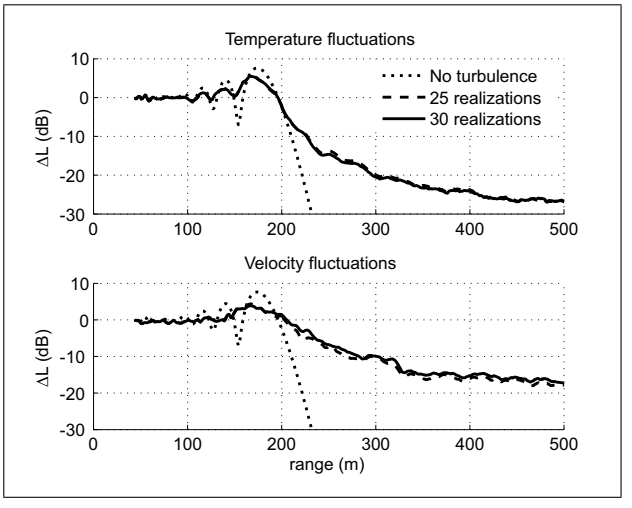

Figure 10. Relative sound pressure level ΔL at a height of 25 m and on the 1600 Hz third octave band for temperature (top) and velocity (bottom) fluctuations. ΔL is calculated by averaging over 25 and 30 realizations of turbulence ($K_{min} = 0.10\,\mathrm{m}^{-1}$ and $K_{max} = 32\,\mathrm{m}^{-1}$).

3.2. Estimate of the maximum cut-off turbulent wave number

The influence of small turbulent structures is studied comparing PE simulations with different maximum turbulent wave numbers K_{max}, K_{min} being set to $0.15\,\mathrm{m}^{-1}$. (It will be show in section 3.3 than turbulent structures with wave numbers smaller than $0.15\,\mathrm{m}^{-1}$ are relatively unimportant for acoustic scattering). The relative sound pressure level on the 400 Hz third octave band for a receiver height of 1 m is plotted in Figure 11. For the reference simulation with $K_{max} = 100\,\mathrm{m}^{-1}$, turbulence effects can be observed at ranges greater than 150 m approximately, corresponding to the shadow zone. At these ranges the relative sound pressure level remains relatively constant. When K_{max} is decreased below a given threshold, scattering by turbulent structures becomes weaker and the sound pressure level in the shadow zone does not reach the reference level corresponding to $K_{max} = 100\,\mathrm{m}^{-1}$; this is the case for $K_{max} \leq 4\,\mathrm{m}^{-1}$ in this particular example. Figure 12 shows the evolution of the relative sound pressure level with respect to height at a range of 300 m for the same set of simulations. As height increases, simulations with lower K_{max}

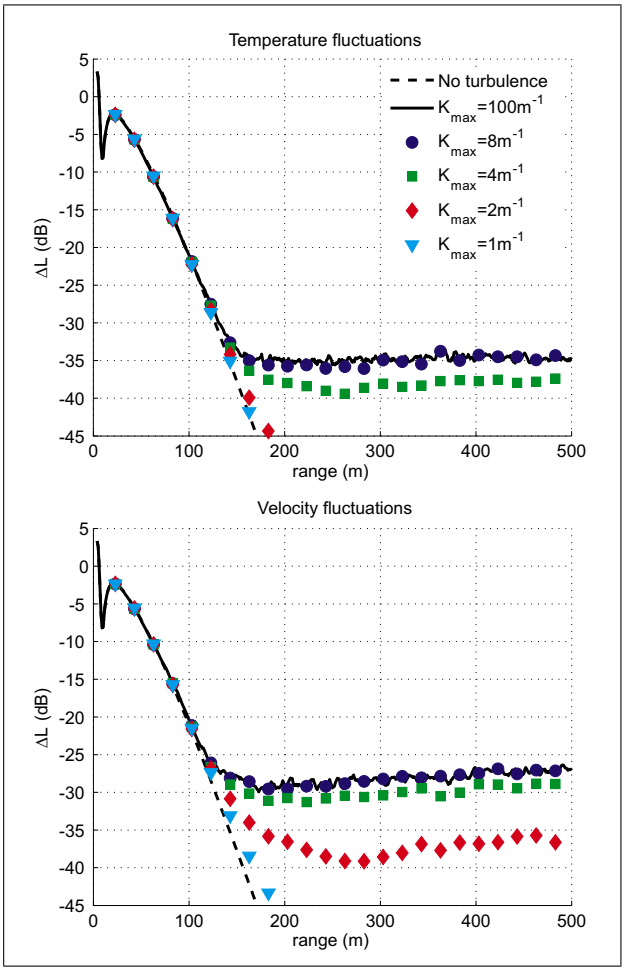

Figure 11. Relative sound pressure level ΔL at a height of 1 m and on the 400 Hz third octave band for temperature (top) and velocity (bottom) fluctuations.

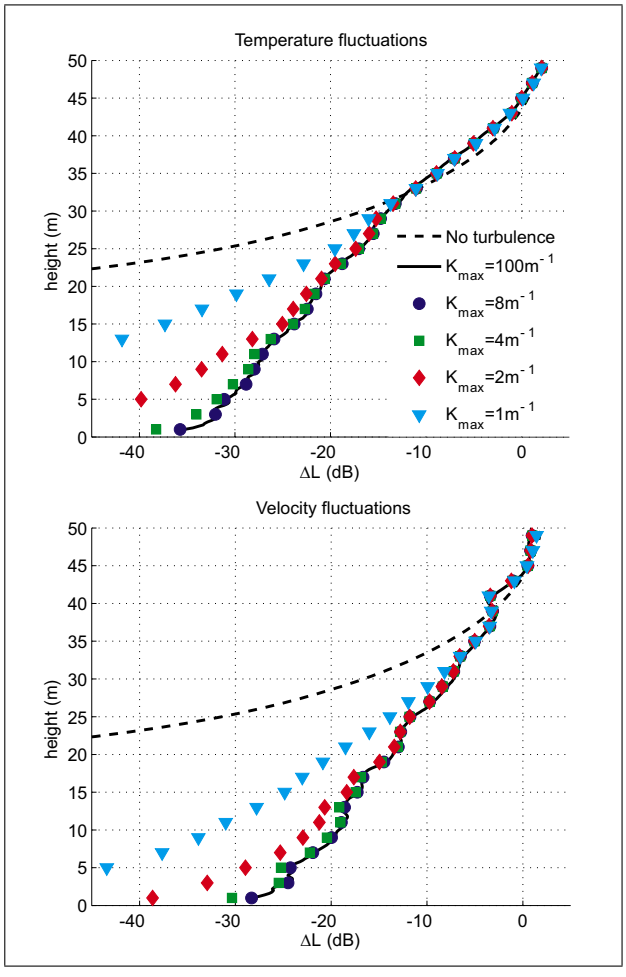

Figure 12. Relative sound pressure level ΔL at a range of 300 m and on the 400 Hz third octave band for temperature (top) and velocity (bottom) fluctuations.

Table II. Estimates of the slope α in $K_{Cmax} = \alpha f$ in terms of the sound speed c_0 at a range of 500 m.

	Temperature fluctuations		Velocity fluctuations	
Receiver height	1 m	10 m	1 m	10 m
Slope α	$6.0c_0$	$3.5c_0$	$5.7c_0$	$3.5c_0$

are in better agreement with the reference solution. For instance, the simulation with $K_{max} = 2\,\mathrm{m}^{-1}$ yields a level 10 dB lower than the reference level at a height of 1 m, but within 1 dB from the reference level at a height of 20 m. As a result, the maximum cut-off wave number K_{Cmax} should be estimated at the greatest range and at the smallest height considered. On the 400 Hz third octave band, $8\,\mathrm{m}^{-1}$ would be a good estimate for K_{Cmax}.

To study the dependence of K_{Cmax} on acoustic frequency, the third octave band spectrum of the relative sound pressure level at a range of 500 m and a height of 1 m is plotted in Figure 13. When acoustic frequency increases, K_{max} must increase so that the sound pressure level remains close to the reference level, which means that the maximum cut-off wave number K_{Cmax} increases with acoustic frequency. This behavior can be explained by the form of the scattering cross-section with respect to scattering angle θ or turbulent wave number K, plotted in Figure 14 at 200 Hz and 1600 Hz. Bragg's relation $K = 2k \sin\theta/2$ is used to relate scattering angle and turbulent wave number. For a given scattering angle, higher turbulent wave numbers are involved when acoustic frequency increases, which explains why K_{Cmax} increases with acoustic frequency. Considering all possible scattering angles, Bragg's relation yields $K \leq 2k$ and $K_{Cmax} = 2k = 4\pi f/c_0$.

The linear dependence $K_{Cmax} = \alpha f$ is also found in the PE simulations. Table II gives estimates of the slope α at a range of 500 m and heights of 1 and 10 m. On a given third octave band, K_{Cmax} is taken as the smallest K_{max} whose associated relative sound pressure level is within 1 dB from the reference level. The results are plotted in Figure 15 for a receiver height of 1 m. For instance, on the 1000 Hz third octave band, Figure 13 shows that the simulation with $K_{max} = 16\,\mathrm{m}^{-1}$ is the only simulation whose level is within 1 dB from the reference level for both temperature and velocity fluctuations. As a re-

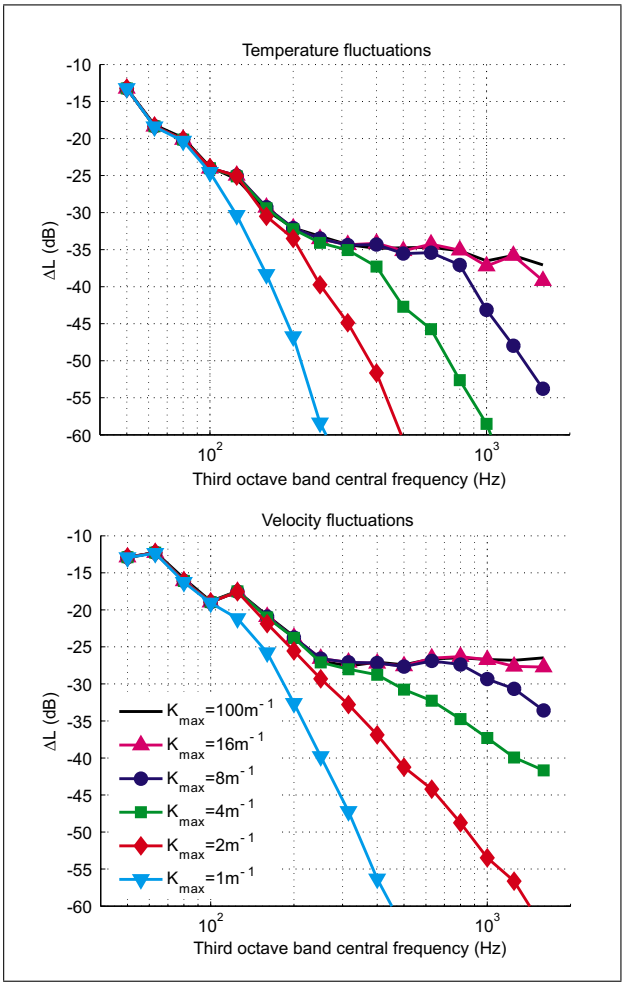

Figure 13. Third octave band spectrum of the relative sound pressure level ΔL at a range of 500 m and a height of 1 m for temperature (top) and velocity (bottom) fluctuations.

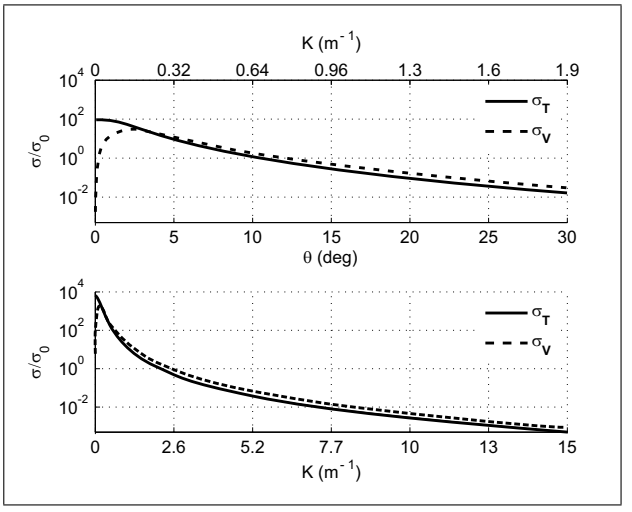

Figure 14. Scattering cross-section for temperature and velocity fluctuations at 200 Hz (top) and 1600 Hz (bottom). The turbulent wave number K is related to the scattering angle θ using Bragg's relation $K = 2k \sin\theta/2$.

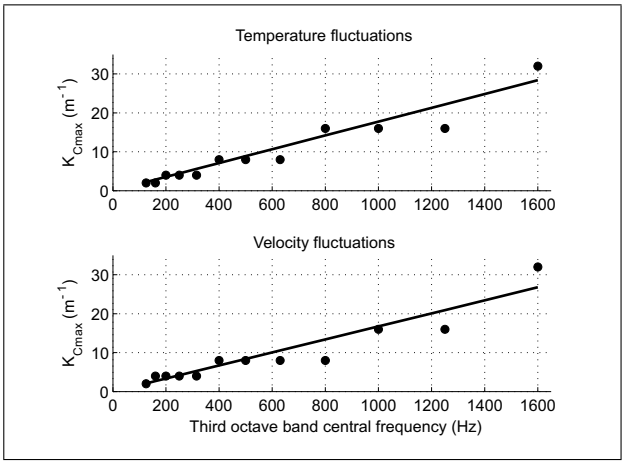

Figure 15. Third octave band spectrum of the maximum cut-off turbulent wave number K_{Cmax} estimated from PE simulations at a receiver height of 1 m. The best fit lines are also plotted.

sult, K_{Cmax} is equal to 16 m^{-1} on the 1000 Hz third octave band. The largest value of K_{Cmax} is 32 m^{-1} on the 1600 Hz third octave band, showing that turbulent structures with wave numbers larger than 32 m^{-1} are not needed in the problem considered. The slope α is estimated using a least square method (see the best fit lines in Figure 15). Values of αc_0 around 6 and 3.5 are found for receiver heights of 1 m and 10 m, respectively. This decrease of α with increasing receiver height is in good agreement with the trend observed in Figure 12 on the 400 Hz third octave band. At both heights, αc_0 is below the theoretical value of 4π given by Bragg's relation considering all possible scattering angles. This difference can be attributed to large scattering angles that are redirecting acoustic energy away from the receiver. For modelling purposes, the maximum cut-off turbulent wave number can be estimated using

$$K_{Cmax} = \frac{4\pi}{c_0} f, \tag{26}$$

even though K_{Cmax} is likely to be smaller than this value. In this section, results are given for temperature and velocity fluctuations separately. Although sound pressure levels in the shadow zone are higher for velocity fluctuations than for temperature fluctuations, estimates of K_{Cmax} appear to be the same, which means that both types of small-scale fluctuations have the same scattering properties.

3.3. Estimate of the minimum cut-off turbulent wave number

The influence of large turbulent structures is studied comparing PE simulations with different minimum turbulent wave numbers K_{min}, K_{max} being set to 32 m^{-1}. Let's introduce the error $Err(K_{min}) = |L_p(K_{min}) - L_{p,ref}|$ where $L_{p,ref}$ is the sound pressure level of the reference simulation with $K_{min} = 0.05\ m^{-1}$. The error $Err(K_{min})$ is an indicator of the influence of turbulent structures whose associated wave numbers are between 0.05 m^{-1} and K_{min}. Maps of the relative sound pressure level for the reference simulation and of the error $Err(0.9\ m^{-1})$ on the 400 Hz

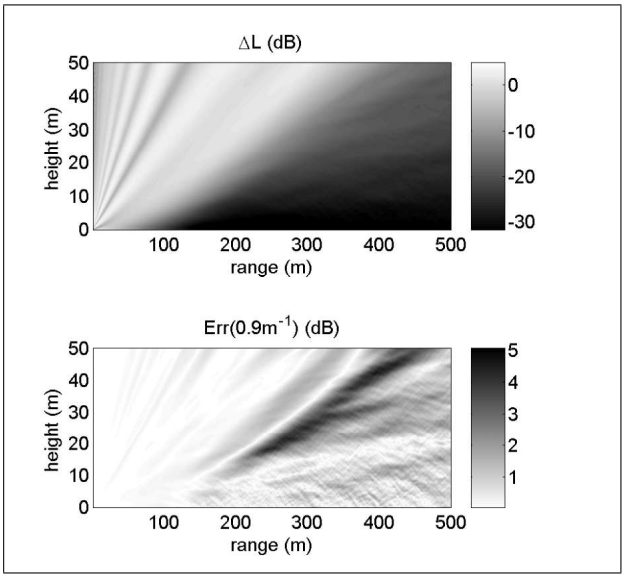

Figure 16. Relative sound pressure level ΔL for the reference simulation ($K_{min} = 0.05\,\mathrm{m}^{-1}$) (top) and error $Err(0.9\,\mathrm{m}^{-1})$ (bottom) on the 400 Hz third octave band for temperature fluctuations.

third octave band are plotted in Figure 16. These maps give a clear indication of the region where large-scale fluctuations have the most influence. It appears that the error is largest in the transition region between the illuminated region and the shadow zone, called the penumbra region. For instance, at a range of 300 m and a height of 25 m, $Err(0.9\,\mathrm{m}^{-1})$ is about 5 dB. Deep in the shadow zone (close to the ground), the error is significantly lower. Although maps in Figure 16 correspond to temperature fluctuations, similar results are obtained with velocity fluctuations.

To estimate the minimum cut-off wave number K_{Cmin}, the maximum of the error over the computation domain, noted $max[Err(K_{min})]$, is used. The computation domain is 500 m long and 50 m high for third octave bands above 160 Hz, as seen in Figure 16. For third octave bands below 125 Hz, the propagation distance is extended to 1 km so that the shadow zone is completely included in the domain, as explained in section 3.1. The spectrum of the maximum error $max[Err(K_{min})]$ is plotted in Figure 17. One can notice that the simulation with $K_{min} = 0.1\,\mathrm{m}^{-1}$ yields small maximum errors over the entire spectrum. One can wonder next if a higher value of K_{min} would be acceptable. Up to 400 Hz approximately, the maximum errors are seen to decrease when acoustic frequency increases, which means that less and less large-scale fluctuations play a significant role, or else that K_{Cmin} increases when acoustic frequency increases. Above 400 Hz, the maximum errors do not follow a clear trend.

In section 2.4, it was shown that turbulent wave numbers much smaller than K_1, or equivalently much smaller than the Fresnel wave number $K_F = \sqrt{2\pi}/\sqrt{\lambda r}$, do not contribute to the variance of log-amplitude fluctuations calculated in the Rytov approximation. Thus it would make sense to look for an estimate of the minimum cut-off turbulent wave number under the form $K_{Cmin} = \beta K_F$, with β to be determined. At high frequencies and for long ranges, the scattering is saturated (see Figure 5) and this relation might not be valid anymore. In Figure 18, the maximum error is calculated over the domain where the Rytov approximation is valid, i.e. $r \leq r_{sat}$, with r_{sat} given in equation (16); the domain height is still 50 m. Compared to Figure 17, the maximum error now keeps on decreasing when acoustic frequency increases above 400 Hz. Note, however, that the computation domain is significantly reduced above 800 Hz, since r_{sat} is about 100 m at these frequencies. As a result, the deep shadow zone might not be reached at high frequencies.

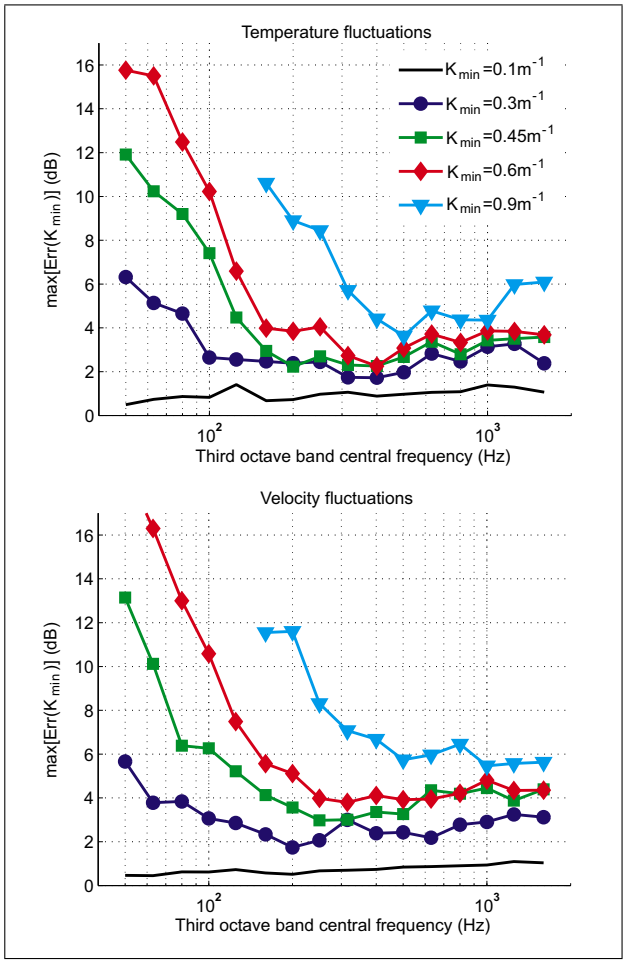

Figure 17. Third octave band spectrum of the maximum of $Err(K_{min})$ for temperature (top) and velocity (bottom) fluctuations. Below 125 Hz, the maximum is calculated over a range of 1000 m and a height of 50 m; above 160 Hz, the maximum is calculated over a range of 500 m and a height of 50 m.

The minimum cut-off turbulent wave number K_{Cmin} is taken as the largest K_{min} whose associated maximum error is less than 2 dB. These estimates are plotted with dots in Figure 19. For instance, for temperature fluctuations on the 400 Hz third octave band, Figure 18 shows that maximum errors are less than 2 dB for the simulations with $K_{min} \leq 0.6\,\mathrm{m}^{-1}$. Thus the estimate of K_{Cmin} is $0.6\,\mathrm{m}^{-1}$ in this case, as seen in Figure 19. Seven PE simulations

have been performed with minimum wave numbers 0.1, 0.2, 0.3, 0.45, 0.6, 0.9, and 1.2 m^{-1}, which explains why the estimated K_{Cmin} curve has a "staircase" look. The estimates of K_{Cmin} are globally seen to increase with acoustic frequency. At low frequency, K_{Cmin} remains constant at 0.1 m^{-1}, which can be attributed to the weak energy associated with turbulent structures whose wave numbers are lower than 0.1 m^{-1} (see the turbulent spectra plotted in Figure 2).

The estimates of K_{Cmin} are compared to βK_F, K_F being calculated with the same range as in the PE simulations, i.e. 1000 m below 125 Hz, 500 m between 160 Hz and 250 Hz, and r_{sat} above 315 Hz ($r_{sat} < 500\,m$ above 315 Hz). The coefficient β has to be small enough such that βK_F remains lower or equal to the estimated value of K_{Cmin} over the entire spectrum. This is the case with $\beta = 1$ for both temperature and velocity fluctuations, as seen in Figure 19, even though estimates of K_{Cmin} are significantly lower for velocity fluctuations than for temperature fluctuations at high acoustic frequency. This difference might be due do the stronger amplitude variations induced by velocity fluctuations with respect to those induced by temperature fluctuations (see for instance the log-amplitude variance $\overline{\chi^2}$ for both types of fluctuations in Figure 8). This would explain that the maximum error in Figure 18 is usually greater for velocity fluctuations than for temperature fluctuations for a given K_{min}. In practice, the minimum cut-off turbulent wave number can be estimated using

$$K_{Cmin} = K_F, \tag{27}$$

as long as the Rytov approximation is valid. It is interesting to see that the filtering function f_χ for log-amplitude fluctuations plotted in Figure 7 is very small for $K < K_F$. Since velocity fluctuations induce stronger acoustic amplitude fluctuations than temperature fluctuations, it might be necessary to take $\beta < 1$ for velocity fluctuations.

4. Summary

Coupling between turbulent scales, geometry and acoustic frequency has been studied in order to estimate the extent of the turbulence spectrum that contributes to acoustic scattering into a refractive shadow zone. This is done in the context of traffic and industrial noise propagation, with the perspective of predicting the sound pressure level variability in the deep shadow zone in relation to the turbulent fluctuations of the atmosphere [25]. PE simulations have been performed in third octave bands between 50 Hz and 1600 Hz to study the influence of small and large-scale turbulent fluctuations. They show that smaller turbulent structures are needed when the receiver is closer to the ground. It also appears that the maximum cut-off turbulent wave number increases linearly with acoustic frequency, which is in agreement with Bragg's relation. Equation (26) can be used to estimate the maximum cut-off turbulent wave number K_{Cmax}.

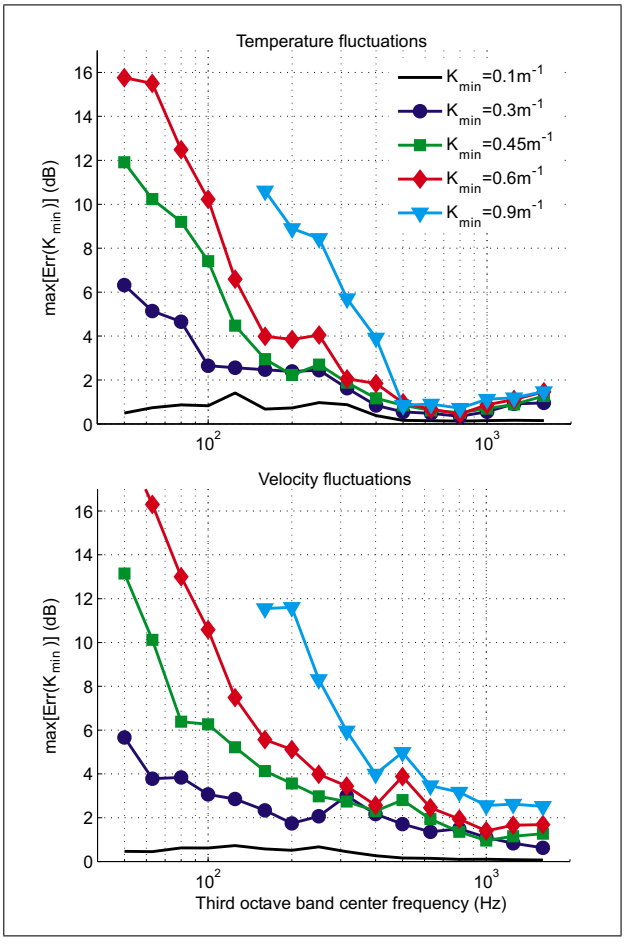

Figure 18. Third octave band spectrum of the maximum of $Err(K_{min})$ for temperature (top) and velocity (bottom) fluctuations. The maximum is calculated over the domain where the Rytov approximation is valid, i.e. $r \leq r_{sat}$.

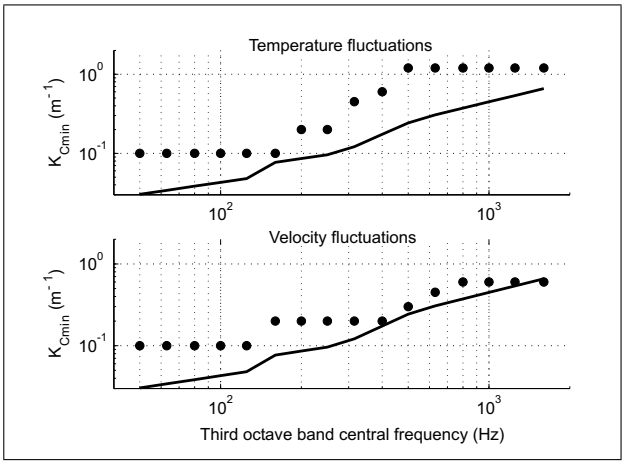

Figure 19. Third octave band spectrum of the minimum cut-off turbulent wave number K_{Cmin} estimated from PE simulations with the condition $r \leq r_{sat}$ on the range. The solid lines corresponds to βK_F with $\beta = 1$.

PE simulations show that large turbulent structures play a significant role in the penumbra region. When the Rytov approximation is valid, the minimum cut-off turbulent

wave number K_{Cmin} is seen to increase with acoustic frequency. It can be estimated using equation (27). When the Rytov approximation is not valid anymore, multipathing occurs and equation (27) breaks down. In this case, all the large-scale fluctuations with significant energy in the turbulence spectrum must be kept; this is the case with $K_{min} = 0.1\,\mathrm{m}^{-1}$ for the turbulent spectra used in this study. Further work is needed to study the influence of large-scale fluctuations in the saturated scattering regime.

Two basic assumptions used in this work are not met in a real atmosphere: the two-dimensional geometry on the one hand, and the isotropy and homogeneity of turbulence on the other hand. PE simulations are performed in a two-dimensional domain to keep the computation time acceptable. As shown in the Appendix, scattering properties in two and three dimensions are very similar using a modified von Kármán spectrum. Thus it is reasonable to say that the estimates of the smallest or largest turbulent scales involved in acoustic scattering are the same in a two or three-dimensional domain. The modified von Kármán spectrum used to model temperature and velocity fluctuations correspond to an idealistic atmosphere. In a real atmosphere, it has been shown that the assumptions of isotropy and homogeneity break down for the large turbulent scales of the energy-containing subrange [10, 12, 17, 26]. This is particularly important for phase fluctuations, but since this would change the scattering properties of turbulence, this might change the coupling between turbulent scales, geometry and acoustic frequency too.

The estimates given in this paper can be useful in numerical simulations to model the relevant part of the turbulence spectrum in a given configuration. They can also be used to know if the range of turbulent scales associated with some wind speed or temperature measurements is large enough for acoustic propagation purposes. In the future, experimental campaigns where consecutive acoustic and environmental measurements were performed could be analyzed in view of the results presented in this paper [25].

Appendix

In section 2, three-dimensional expressions for the scattering cross-section and the variance of log-amplitude and phase fluctuations in the Rytov approximation have been presented. These results are well-known in the literature, while similar expressions in a two-dimensional space can hardly be found. The derivation and formula for the sound scattering cross-section in two dimensions are presented in Appendix A2. The classical derivation in the three-dimensional case is also given since the basic steps in both derivations are the same. The expression for the variance of log-amplitude and phase fluctuations in the Rytov approximation is given in Appendix A3. The derivation has been done by Chevret [27], and is not repeated here. For both the scattering cross-section and the variances of log-amplitude and phase fluctuations, two and three-dimensional expressions are compared, showing that scattering properties are similar in both cases.

A1. Turbulence modelling

The spectral density has the same dependence in turbulent wave number in two and three dimensions [27]. In the Markov approximation, the two-dimensional spectra of thermal turbulent energy $G^{2D}(K)$ and kinetic turbulent energy $E^{2D}(K)$ are related to the spectral density $\Phi_n^{2D}(K)$ by

$$\Phi_n^{2D}(K) = \frac{1}{4T_0^2}\frac{G^{2D}(K)}{\pi K} + \frac{1}{c_0^2}\frac{E^{2D}(K)}{\pi K}. \tag{A1}$$

Thus, for the modified von Kármán spectrum:

$$G^{2D}(K) = C\frac{\overline{T'^2}}{L_0^{5/3}} K \left(K^2 + \frac{1}{L_0^2}\right)^{-11/6} \mathrm{e}^{-K^2/K_m^2}, \tag{A2}$$

$$E^{2D}(K) = \frac{11}{6} C\frac{\overline{V_x'^2}}{L_0^{5/3}} K^3 \left(K^2 + \frac{1}{L_0^2}\right)^{-17/6} \mathrm{e}^{-K^2/K_m^2}, \tag{A3}$$

with $C = 5/3$, and with the notations of section 2.1.

A2. Scattering cross-section

The derivation starts from the inhomogeneous Helmholtz equation for the scattered pressure p_s:

$$\nabla^2 p_s + k^2 p_s = -\gamma(\mathbf{r}) p_s, \tag{A4}$$

with

$$\gamma(\mathbf{r}) = -k^2\frac{T'}{T_0} + \nabla\left(\frac{T'}{T_0}\right)\nabla - \frac{2\mathrm{i}}{c_0 k}\frac{\partial V_i'}{\partial x_j}\frac{\partial^2}{\partial x_i \partial x_j} + \frac{2\mathrm{i}k}{c_0}\mathbf{V}'\cdot\nabla. \tag{A5}$$

This expression for $\gamma(\mathbf{r})$ is derived from Ostashev's work (see equation (7.1) of [5]) keeping only temperature and velocity fluctuations. If the pressure field is single scattered by the temperature and velocity fields, p_s on the right-hand side of equation (A4) can be replaced by the incident pressure p_0. Using an integral formulation:

$$p_s(\mathbf{r}) = \int_{L^n} \gamma(\mathbf{r}') p_0(\mathbf{r}') G(\mathbf{r}, \mathbf{r}')\, \mathrm{d}^n\mathbf{r}', \tag{A6}$$

where n is 3 in 3D and 2 in 2D, and $G(\mathbf{r}, \mathbf{r}')$ is the associated Green's function. Notations of Figure 3 are used, and L is the linear size of the scattering volume. The Green's function is:

$$G(\mathbf{r}, \mathbf{r}') = \begin{cases} (4\pi|\mathbf{r}-\mathbf{r}'|)^{-1}\exp(\mathrm{i}k|\mathbf{r}-\mathbf{r}'|) & \text{in 3D,} \\ \frac{\mathrm{i}}{4}H_0^{(2)}(k|\mathbf{r}-\mathbf{r}'|) & \text{in 2D,} \end{cases} \tag{A7}$$

with $H_0^{(2)}$ the Hankel function of second kind and of order zero. Assuming $p_0(\mathbf{r}) = A_0\exp(\mathrm{i}k\mathbf{m_0}\cdot\mathbf{r})$ for the incident wave, the derivatives of the $\gamma(\mathbf{r}')p_0(\mathbf{r}')$ term are written:

$$\frac{\partial \exp(\mathrm{i}k\mathbf{m_0}\cdot\mathbf{r}')}{\partial x_j'} = \mathrm{i}k m_{0,j}\exp(\mathrm{i}k\mathbf{m_0}\cdot\mathbf{r}'), \tag{A8}$$

with $\mathbf{m_0} = -\mathbf{r_0}/r_0$. Thus $\gamma(\mathbf{r})$ in equation (A6) becomes:

$$\gamma(\mathbf{r}) = -k^2\frac{T'}{T_0} + \mathrm{i}k\mathbf{m_0}\cdot\nabla\left(\frac{T'}{T_0}\right) + \frac{2\mathrm{i}k}{c_0}(\mathbf{m_0}\cdot\nabla)(\mathbf{m_0}\cdot\mathbf{V}') - \frac{2k^2}{c_0}(\mathbf{m_0}\cdot\mathbf{V}'). \quad \text{(A9)}$$

In the far-field approximation ($r \gg L$), $|\mathbf{r}-\mathbf{r}'| \approx r - \mathbf{m}\cdot\mathbf{r}'$, where $\mathbf{m} = \mathbf{r}/r$, and

$$H_0^{(2)}\left(k|\mathbf{r}-\mathbf{r}'|\right) \approx \frac{\sqrt{2}}{\sqrt{\pi k|\mathbf{r}-\mathbf{r}'|}}\exp\left(\mathrm{i}k|\mathbf{r}-\mathbf{r}'| - \mathrm{i}\pi/4\right).$$

Equations (A6) and (A7) thus yield:

$$p_s^{3D}(\mathbf{r}) = \frac{A_0\mathrm{e}^{\mathrm{i}kr}}{4\pi r}\int_V \gamma(\mathbf{r}')\mathrm{e}^{\mathrm{i}k(\mathbf{m_0}-\mathbf{m})\cdot\mathbf{r}'}\,\mathrm{d}^3\mathbf{r}', \quad \text{(A10)}$$

in three dimensions, and

$$p_s^{2D}(\mathbf{r}) = \frac{A_0\mathrm{i}\mathrm{e}^{\mathrm{i}kr-\mathrm{i}\pi/4}}{2\sqrt{2\pi kr}}\int_S \gamma(\mathbf{r}')\mathrm{e}^{\mathrm{i}k(\mathbf{m_0}-\mathbf{m})\cdot\mathbf{r}'}\,\mathrm{d}^2\mathbf{r}', \quad \text{(A11)}$$

in two dimensions, with S the scattering surface. Furthermore, Ostashev [5] shows that for $r, r_0 \gg L \gg \lambda$:

$$\int_{L^n}(\mathbf{m_0}\cdot\nabla')\eta(\mathbf{r}')\mathrm{e}^{\mathrm{i}k(\mathbf{m_0}-\mathbf{m})\cdot\mathbf{r}'}\mathrm{d}^n\mathbf{r}' \approx -\int_{L^n}\eta(\mathbf{r}')\mathrm{i}k(1-\mathbf{m_0}\cdot\mathbf{m})\mathrm{e}^{\mathrm{i}k(\mathbf{m_0}-\mathbf{m})\cdot\mathbf{r}'}\,\mathrm{d}^n\mathbf{r}'. \quad \text{(A12)}$$

This approximation applies to the second and third terms of equation (A9). As a result, $\gamma(\mathbf{r})$ in equations (A10) and (A11) now reads, using $\mathbf{m_0}\cdot\mathbf{m} = \cos\theta$ (see Figure 3):

$$\gamma(\mathbf{r}) = -k^2\cos\theta\left[\frac{T'}{T_0} + \frac{2}{c_0}(\mathbf{m_0}\cdot\mathbf{V}')\right]. \quad \text{(A13)}$$

Let $\Gamma(\mathbf{K})$ be the Fourier transform of $\gamma(\mathbf{r})$, defined here as:

$$\Gamma^{3D}(\mathbf{K}) = \frac{1}{8\pi^3}\int_V \gamma(\mathbf{r})\mathrm{e}^{-\mathrm{i}\mathbf{K}\cdot\mathbf{r}}\mathrm{d}^3\mathbf{r}, \quad \text{(A14)}$$

$$\Gamma^{2D}(\mathbf{K}) = \frac{1}{4\pi^2}\int_S \gamma(\mathbf{r})\mathrm{e}^{-\mathrm{i}\mathbf{K}\cdot\mathbf{r}}\mathrm{d}^2\mathbf{r}, \quad \text{(A15)}$$

in three and two dimensions, respectively. Using equations (A10) and (A11), the scattered pressure can be written as a function of Γ:

$$p_s^{3D}(\mathbf{r}) = 2\pi^2\frac{A_0\mathrm{e}^{\mathrm{i}kr}}{r}\Gamma^{3D}(-\mathbf{q}), \quad \text{(A16)}$$

$$p_s^{2D}(\mathbf{r}) = \mathrm{i}\sqrt{2}\pi^2\frac{A_0\mathrm{e}^{\mathrm{i}kr-\mathrm{i}\pi/4}}{\sqrt{\pi kr}}\Gamma^{2D}(-\mathbf{q}), \quad \text{(A17)}$$

with $\mathbf{q} = k(\mathbf{m_0}-\mathbf{m})$. The mean scattered intensity is proportional to $\overline{p_s p_s{}^*}(\mathbf{r})$, where * means "complex conjugate of". Thus $\overline{\Gamma\Gamma^*}(\mathbf{q})$ needs to be calculated next; it can be related to the spectral densities of temperature fluctuations Φ_T and of velocity fluctuations Φ_{ij} using equation (A13).

In three dimensions:

$$\overline{\Gamma^{3D}\Gamma^{3D*}}(-\mathbf{q}) = \frac{k^4\cos^2\theta}{(8\pi^3)^2}\int_V \mathrm{d}^3\mathbf{r}'\int_V\left(\frac{\overline{T'(\mathbf{r}')T'(\mathbf{r}'+\mathbf{\Delta r}')}}{T_0^2} + 4m_{0,i}m_{0,j}\frac{\overline{V_i'(\mathbf{r}')V_j'(\mathbf{r}'+\mathbf{\Delta r}')}}{c_0^2}\right)\mathrm{e}^{-\mathrm{i}\mathbf{q}\cdot\mathbf{\Delta r}'}\mathrm{d}^3\mathbf{r}'', \quad \text{(A18)}$$

with $\mathbf{\Delta r}' = \mathbf{r}'' - \mathbf{r}'$. This result is obtained supposing the temperature and velocity fields are uncorrelated. The correlation functions of temperature and velocity fluctuations appear in equation (A18). They are the inverse Fourier transforms of the corresponding spectral densities, thus:

$$\overline{\Gamma^{3D}\Gamma^{3D*}}(-\mathbf{q}) = \frac{V}{8\pi^3}k^4\cos^2\theta \cdot\left[\frac{\Phi_T^{3D}(\mathbf{q})}{T_0^2} + 4m_{0,i}m_{0,j}\frac{\Phi_{ij}^{3D}(\mathbf{q})}{c_0^2}\right]. \quad \text{(A19)}$$

Combining equations (6), (A16) and (A19):

$$\sigma^{3D}(\mathbf{q}) = \frac{r^2\overline{p_s^{3D}p_s^{3D*}}(\mathbf{r})}{A_0^2V} = \frac{4\pi^4\overline{\Gamma^{3D}\Gamma^{3D*}}(-\mathbf{q})}{V} = 2\pi k^4\cos^2\theta\left[\frac{\Phi_T^{3D}(\mathbf{q})}{4T_0^2} + m_{0,i}m_{0,j}\frac{\Phi_{ij}^{3D}(\mathbf{q})}{c_0^2}\right]. \quad \text{(A20)}$$

In equation (7) presented in section 2.2, the scattering cross-section is expressed as a function of the turbulent energy spectra. This is straightforward noting that $|\mathbf{q}| = 2k\sin\theta/2$ for homogeneous and isotropic turbulence, and using

$$\Phi_T^{3D}(K) = \frac{G^{3D}(K)}{4\pi K^2}, \quad \text{(A21)}$$

$$\Phi_{ij}^{3D}(K) = \left(\delta_{ij} - \frac{K_iK_j}{K^2}\right)\frac{E^{3D}(K)}{4\pi K^2}. \quad \text{(A22)}$$

The two-dimensional scattering cross-section is defined as:

$$\sigma^{2D} = \frac{r\bar{I}_s}{I_0S}. \quad \text{(A23)}$$

Following the same steps as in the three-dimensional case, one obtains:

$$\overline{\Gamma^{2D}\Gamma^{2D*}}(-\mathbf{q}) = \frac{S}{4\pi^2}k^4\cos^2\theta \cdot\left[\frac{\Phi_T^{2D}(\mathbf{q})}{T_0^2} + 4m_{0,i}m_{0,j}\frac{\Phi_{ij}^{2D}(\mathbf{q})}{c_0^2}\right]. \quad \text{(A24)}$$

Combining equations (A16), (A23) and (A24):

$$\sigma^{2D}(\mathbf{q}) = \frac{r\overline{p_s^{2D}p_s^{2D*}}(\mathbf{r})}{A_0^2S} = \frac{2\pi^3\overline{\Gamma^{2D}\Gamma^{2D*}}(-\mathbf{q})}{kS} = 2\pi k^3\cos^2\theta\left[\frac{\Phi_T^{2D}(\mathbf{q})}{4T_0^2} + m_{0,i}m_{0,j}\frac{\Phi_{ij}^{2D}(\mathbf{q})}{c_0^2}\right]. \quad \text{(A25)}$$

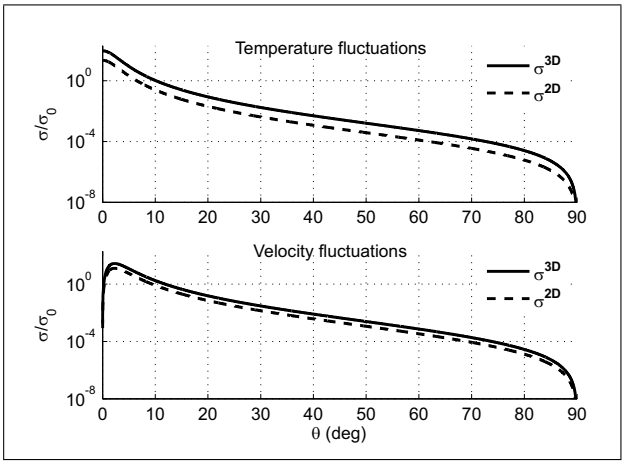

Figure A1. Normalized cross-section σ/σ_0 at 200 Hz for temperature (top) and velocity (bottom) fluctuations in two and three dimensions.

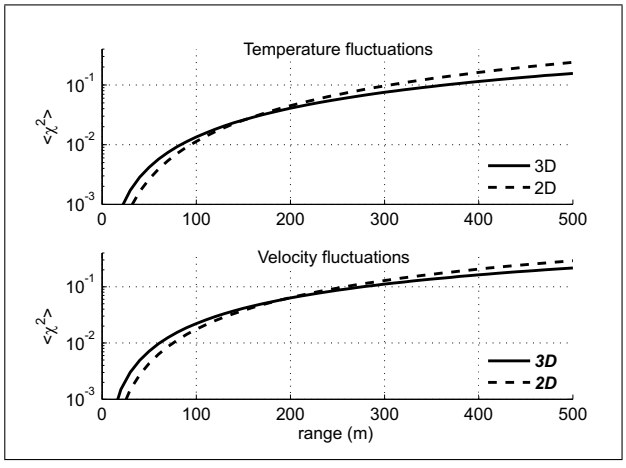

Figure A2. Variance of log-amplitude fluctuations $\overline{\chi^2}$ in the Rytov approximation at 200 Hz for temperature (top) and velocity (bottom) fluctuations in two and three dimensions.

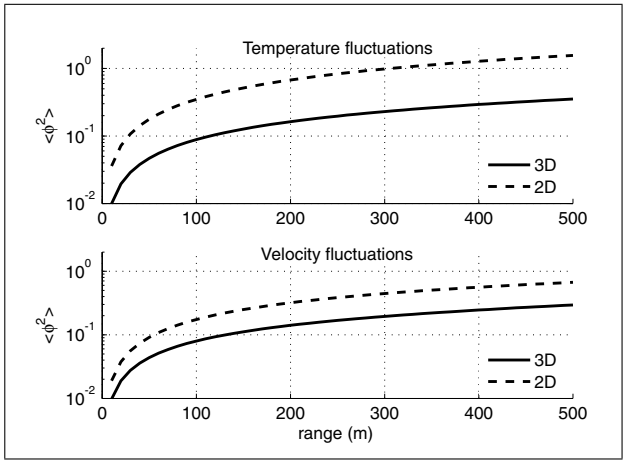

Figure A3. Variance of phase fluctuations $\overline{\phi^2}$ in the Rytov approximation at 200 Hz for temperature (top) and velocity (bottom) fluctuations in two and three dimensions.

For homogeneous and isotropic turbulence, the scattering cross-section can be expressed as a function of the turbulent energy spectra using

$$\Phi_T^{2D}(K) = \frac{G^{2D}(K)}{\pi K}, \tag{A26}$$

$$\Phi_{ij}^{2D}(K) = \left(\delta_{ij} - \frac{K_i K_j}{K^2}\right) \frac{E^{2D}(K)}{\pi K}. \tag{A27}$$

This yields:

$$\sigma^{2D}(\theta) = k^2 \frac{\cos^2\theta}{\sin\theta/2} \left[\frac{1}{4T_0^2} G^{2D}(2k sin\theta/2) + \frac{\cos^2\theta/2}{c_0^2} E^{2D}(2k sin\theta/2)\right]. \tag{A28}$$

Equation (A28) is the two-dimensional equivalent to equation (7). Both expressions have similar forms. Using equations (A2) and (A3), an analytical expression can be derived for the two-dimensional scattering cross-section associated with a modified von Kármán spectrum:

$$\sigma^{2D}(\theta) = \frac{2^{-14/3} C L_0^{-5/3} k^{-2/3} \cos^2\theta}{\left(\sin^2\theta/2 + (2kL_0)^{-2}\right)^{11/6}} D(k,\theta) \cdot \left[\frac{\overline{T'^2}}{T_0^2} + \frac{11}{6}\frac{\overline{V_x'^2}}{c_0^2} \frac{\sin^2\theta}{\sin^2\theta/2 + (2kL_0)^{-2}}\right], \tag{A29}$$

where $D(k,\theta)$ is the same as in equation (8). The scattering cross-section is normalized by the total scattering cross-section, which is:

$$\sigma_0^{2D} = \int_0^{2\pi} \sigma^{2D}(\theta)\, d\theta, \tag{A30}$$

in a two-dimensional domain. Comparing equations (8) and (A29), it appears that the scattering cross-section is very similar in two and three dimensions. This similarity can be observed in Figure A1, where both expressions of the normalized scattering cross-section are plotted at 200 Hz. The angular dependence is the same in two and three dimensions, even though the scattering is more intense in a three-dimensional domain.

A3. Variance of log-amplitude and phase fluctuations in the Rytov approximation

The variances of log-amplitude and phase fluctuations in two dimensions are written [27]:

$$\overline{\chi^2}, \overline{\phi^2} = 2\pi k^2 r \int_0^\infty f_{\chi,\phi}(K^2/K_F^2)\Phi_n^{2D}(K)\, dK, \tag{A31}$$

with $f_{\chi,\phi}$ given in equation (19) for spherical wave propagation, and Φ_n^{2D} given by equations (A1), (A2) and (A3). Thus the filtering functions $f_{\chi,\phi}$ are the same in two and three dimensions, which means that the coupling between turbulence scales, acoustic frequency and geometry is the same in both cases. The variances of log-amplitude and phase fluctuations in two and three dimensions are evaluated numerically at 200 Hz and compared in Figures A2

and A3. Whereas the variances of log-amplitude fluctuations have similar values in two and three dimensions for both temperature and velocity fluctuations, the variance of phase fluctuations tends to be greater in two dimensions than in three dimensions. This difference can be attributed to stronger components at low wave numbers in the two-dimensional energy spectrum with respect to the three-dimensional energy spectrum.

Acknowledgement

Support by CNRS and SNCF is gratefully acknowledged. This work is done in the framework of the GDR 2493 "Bruit des transports", with the support of the French Ministry of Ecology and Sustainable Development. The authors also thank the reviewers for their constructive comments and suggestions.

References

[1] M. Stinson, D. Havelock, G. Daigle: Simulation of scattering by turbulence into a shadow region using the gf-pe method. Sixth International Symposium on Long Range Sound Propagation, Ottawa, Canada, 1994, 283–295.

[2] V. Tatarski: Wave propagation in a turbulent medium. McGraw-Hill, 1961.

[3] A. Ishimaru: Wave propagation and scattering in random media. Vol. 2. Academic Press, 1979.

[4] S. Rytov, Y. Kravtsov, V. Tatarski: Principles of radiophysics 4: Wave propagation through random media. Springer-Verlag, 1989.

[5] V. Ostashev: Acoustics in moving inhomogeneous media. E and FN SPON, 1997.

[6] Z. Ye: Sound scattering from a moving turbulent medium. J. Acoust. Soc. Am. **102** (1997) 752–758.

[7] V. Ostashev, G. Goedecke, R. Wood, H. Auvermann, S. Clifford: Sound scattering cross-section in a stratified moving atmosphere. J. Acoust. Soc. Am. **105** (1999) 3115–3125.

[8] N. Pan: Excess attenuation of an acoustic beam by turbulence. J. Acoust. Soc. Am. **114** (2003) 3102–3111.

[9] K. Gilbert, X. Di, R. Korte: Distorted-wave born approximation analysis of sound levels in a refractive shadow zone. Seventh International Symposium on Long Range Sound Propagation, Lyon, France, 1996, 373–389.

[10] D. Wilson, J. Brasseur, K. Gilbert: Acoustic scattering and the spectrum of atmospheric turbulence. J. Acoust. Soc. Am. **105** (1999) 30–34.

[11] M. Stinson, G. Daigle: Meteorological measurements for use in sound propagation calculations. Seventh International Symposium on Long Range Sound Propagation, Lyon, France, 1996, 137–147.

[12] D. Wilson, D. Thomson: Acoustic propagation through anisotropic, surface-layer turbulence. J. Acoust. Soc. Am. **96** (1994) 1080–1095.

[13] D. Juvé, P. Blanc-Benon, P. Chevret: Sound propagation through a turbulent atmosphere: Influence of the turbulence model. Sixth International Symposium on Long Range Sound Propagation, Ottawa, Canada, 1994, 270–282.

[14] P. Blanc-Benon, L. Dallois, D. Juvé: Long range sound propagation in a turbulent atmosphere within the parabolic approximation. Acta Acustica united with Acustica **87** (2001) 659–669.

[15] S. Flatté, R. Dashen, W. Munk, K. Watson, F. Zachariasen: Sound transmission through a fluctuating ocean. Cambridge University Press, 1978.

[16] V. Ostashev: Sound propagation and scattering in media with random inhomogeneities of sound speed, density and medium velocity. Waves in Random Media **4** (1994) 403–428.

[17] V. Ostashev, I. Chunchuzov, D. Wilson: Sound propagation through and scattering by internal gravity waves in a stably stratified atmosphere. J. Acoust. Soc. Am. **118** (2005) 3420–3429.

[18] P. Blanc-Benon, D. Juvé: Intensity fluctuations of spherical acoustic waves propagating through thermal turbulence. Waves in Random Media **3** (1993) 71–83.

[19] L. Dallois, P. Blanc-Benon, D. Juvé: A wide-angle parabolic equation for acoustic waves in inhomogeneous moving media: Applications to atmospheric sound propagation. J. Comp. Acoust. **9** (2001) 477–494.

[20] B. Lihoreau, B. Gauvreau, M. Bérengier, P. Blanc-Benon, I. Calmet: Outdoor sound propagation modelling in realistic environments: Application of coupled parabolic and atmospheric models. J. Acoust. Soc. Am. **120** (2006) 110–119.

[21] L. Dallois: Propagation des ondes acoustiques dans les milieux en mouvement: extension grand angle de l'approximation parabolique. Dissertation, École Centrale de Lyon, no. 2000-37, 2000.

[22] L. Dallois, P. Blanc-Benon: Wide angle parabolic equations in moving media: Sound diffraction by a core vortex. Seventh AIAA/CEAS Aeroacoustics Conference, Maastricht, Netherlands, 2001, AIAA Paper 2001–2256.

[23] M. Delany, E. Bazley: Acoustical properties of fibrous absorbent materials. Appl. Acoust. **3** (1970) 105–116.

[24] P. Chevret, P. Blanc-Benon, D. Juvé: A numerical model for sound propagation through a turbulent atmosphere near the ground. J. Acoust. Soc. Am. **100** (1996) 3587–3599.

[25] F. Junker, B. Gauvreau, M. Bérengier, C. Cremezi-Charlet, P. Blanc-Benon, B. Cotté, D. Ecotière: Classification of relative influence of physical parameters for long range acoustic propagation. Internoise 2006, Honolulu, Hawaii, USA, 2006, CD–Rom Proceedings.

[26] K. Wert, P. Blanc-Benon, D. Juvé: Effect of turbulence scale resolution on numerical simulation of atmospheric sound propagation. Fourth AIAA/CEAS Aeroacoustics Conference, Toulouse, France, 1998, AIAA Paper 98–2245, 246–256.

[27] P. Chevret: Simulation numérique des effets de la turbulence sur la propagation du son dans l'atmosphère. Dissertation, École Centrale de Lyon, no. 94-18, 1994.